Proceedings of the ASME 2023
Manufacturing Science and Engineering Conference
MSEC 2023
June 12–16, 2023, New Brunswick, NJ, USA

MSEC2023-104786

THERMAL-IMAGE-ENABLED ADDITIVE MANUFACTURING PROCESS MONITORING AND EXTRUSION TRAJECTORY COMPENSATION

Molong Duan[1,2,*], Siqi Chen[1], Yuexin Yang[1]

[1]Hong Kong University of Science and Technology, Hong Kong SAR, China
[2]HKUST Shenzhen-Hong Kong Collaborative Innovation Research Institute, Futian, Shenzhen, China

ABSTRACT

The additive manufacturing (AM) system today still suffers from low precision, low product stability, low automation level, and low data utilization. The urgent need for enhancements on these fronts leads to the various monitoring and control techniques for AM process. Currently, most existing AM monitoring and corresponding control methods are built on statistical models and used to refine the AM process under a parameter-tuning framework. They help regulate the steady-state or low-frequency behavior in AM process but do not address issues related to AM's unsteady or dynamic behavior. These unsteady and dynamic behaviors are especially prevalent in high-speed, high-acceleration AM systems with moving parts (e.g., fused filament fabrication, directed energy deposition) and dynamic trajectory regions (e.g., corners). Therefore, in this paper, we proposed a monitoring and control solution that addresses printing inaccuracies with real-time thermal image monitoring. The method depends on a low-order analytical model describing the printed path boundary and an established non-contacting deposition direction. The thermal image observations are thus converted to the dynamic time-domain compensation signals to account for dynamic over-extrusion. The method is verified with a fused filament fabrication printer to alleviate its over-extrusion when printing corners.

Keywords: Additive manufacturing, thermal monitoring, thermal image processing, image-based compensation

1. INTRODUCTION

Additive manufacturing (AM), via layer-to-layer fabrication of 3-dimensional (3D) objects, introduces significant flexibility and convenience for prototyping and the manufacturing of parts with complex internal features [1]. However, current AM still suffers from its limitations of low precision, low product stability, low automation level, and low data utilization [2–4]. To improve printing performances and robustness, enhanced levels of monitoring and advanced feedback control methods are needed [2].

In-situ monitoring and feedback are believed to be most effective in enhancing the robustness of the AM processes and thus received extensive academic and industrial focus [4,5]. They are especially effective in the early-stage intervention of various common issues such as porosity and cracks [3]. Currently, five different categories of information [4] are typically used, including existing equipment signals, powder uniformity characteristics, visible/infrared images, spatter traces, and molten area characteristics. The monitoring process serves for the identification of faults, and also aims to timely adjust the printing process. The adjustment typically relies on the model between the AM condition and the observable features. Liu et al. [6] established a macroscopic relationship between feeding parameters and manufacturing quality and used it to optimize the feeding parameters. Lee and Prabhu [7] developed a method for predicting manufacturing quality using heat transfer models. Liu et al. [8] and Gardner et al. [9] established simplified models for the bonding and strength of fused filament fabrication of fiber and DED processes, respectively. Prasad et al. [10] built an experimental data-driven model for the melting process. However, most of these models capture the statistical relationship between the printing performance and the parameters. Therefore, it encourages statistical parameter tuning, but cannot handle the highly dynamic features during the printing process (e.g., vibrations, local over-extrusion, etc.).

With a large amount of data available in the AM process, the dynamic adjustment of the printing process for enhanced

* Corresponding author: duan@ust.hk

performance is still the key [11]. Numerous parameters in additive manufacturing (e.g., printing speed, layer geometry, temperature, feed speed, etc.) make the corresponding control problem to be very complex [12,13]. Machine learning and other artificial intelligence algorithms [14] provide new theoretical tools for these optimization processes. However, the machine learning method used in closed-loop control is still under a low-speed parameter adjustment framework [14–16]. Baturynska et al. [17] proposed a conceptual framework for general parameter adjustment; Zhao et al. [18], Zomorodi et al. [19] and Deuser et al. [20] developed controllers exploiting the contact force, material flow, and printing speed. In addition, various classical controllers, including adaptive control [21], anti-windup PID control [22], fuzzy control [23,24], nonlinear model predictive control [25], etc., have been used to adjust the printing parameters. However, current control methods mainly focus on adjusting the parameters [23], and thus cannot handle the high-frequency dynamics in the critical regions. In addition, the existing efforts have not tried to extract the trajectory and extrusion information from the thermal images, particularly in fused filament fabrication printers where a relatively long temperature history is available.

In this work, we aim to build the dynamic relationship between the extrusion and the printed path geometry, and use this geometrical relationship to optimize the extrusion trajectory, with the help of in-situ thermal images. Section 2 discusses the backgrounds and operations for the camera calibration and distortion compensation. Section 3 proposes a geometric model of the printed path and a method to smooth the curvature to build non-contacting deposition directions. The method to extract the over-extrusion regions and corresponding compensation methods are also introduced. Section 4 introduces the experiment details, including the hardware setup, testing trajectory, extrusion dynamics identification, and the extrusion trajectory compensation results, followed by the conclusion in Section 5.

2. THERMAL IMAGE PROCESSING BACKGROUND

The two main sources of errors in the raw thermal image are camera distortion and the non-vertical view angle. As illustrated in Figure 1(b), the lines near the edges of the image become curved, and the straight lines are also curved and tilt. The following two subsections provide the background and procedures for the thermal camera distortion compensation and view angle calibration.

2.1. Thermal Camera Distortion Compensation and Perspective Transformation

Distortion is an inherent characteristic of the camera lens and is impossible to eliminate completely. For a camera, its distortion coefficient is fixed and can be identified through experiments. In our study, we adopt Zhang's methods [26] for the camera calibration to compensate for the radial and tangential distortion.

Radial distortion arises from the distance difference for different regions of the picture to the lens and is described by

$$x_{dr}^{(im)} = x_0^{(im)}(1 + k_1 r^2 + k_2 r^4 + k_3 r^6), \tag{1}$$

$$y_{dr}^{(im)} = y_0^{(im)}(1 + k_1 r^2 + k_2 r^4 + k_3 r^6), \tag{2}$$

where the point in location $(x_0^{(im)}, y_0^{(im)})$ is distorted to $(x_{dr}^{(im)}, y_{dr}^{(im)})$ under radial distortion; r is the distance to the distortion center, and k_1, k_2, and k_3 are radial distortion coefficients. On the other hand, tangential distortion arises from the mounting deviations from the lens, and is described by parameters p_{t1} and p_{t2} following

$$x_{dt} = x + (2p_{t1}xy + p_{t2}(r^2 + 2x^2)), \tag{3}$$

$$y_{dt} = y + (p_{t1}(r^2 + 2y^2) + 2p_{t2}xy), \tag{4}$$

where (x_{dt}, y_{dt}) is the position of the points after tangential distortion. The radial and tangential distortion compensation is packaged into a camera intrinsic matrix A_t satisfying

$$\begin{bmatrix} x_1^{(im)} \\ y_1^{(im)} \\ 1 \end{bmatrix} = \underbrace{\begin{bmatrix} \alpha_t & c_t & x_t \\ 0 & \beta_t & y_t \\ 0 & 0 & 1 \end{bmatrix}}_{A_t} \begin{bmatrix} x_0^{(im)} \\ y_0^{(im)} \\ 1 \end{bmatrix}, \tag{5}$$

where $(x_1^{(im)}, y_1^{(im)})$ are the compensated coordinates of $(x_0^{(im)}, y_0^{(im)})$, α_t and β_t are the scale factors in image axes, and c_t represents the skewness of the two image axes.

After the radial distortion compensation, perspective transformation addresses the tilt of the camera to the image surface via an additional transformation matrix M_t, following the relationship

$$(x_2, y_2) = (x_1, y_1) M_t. \tag{6}$$

These calibrations typically build upon the data from the training set, where chessboard sample images with known characteristic lengths are used. The perspective transformation in Eq. (6), unlike the radial distortion compensation, strongly depends on the relative location of the camera and the captured image. Therefore, calibration procedures are needed when the camera is removed and reinstalled.

2.2. Calibration Process and Result

To perform the calibration process, we first stuck a metal chessboard with a known and accurate size to the printing bed. More than 10 images were taken from different angles and distances. Secondly, the characteristic points, referring to all internal corner points of the chessboard, are detected for perspective matrix solving. Finally, the intrinsic matrix of the camera and distortion coefficients are calculated. The overall

mean reprojection error $R_e \leq 0.5$ pixel indicates an effective result.

Typically, color cameras can directly display the black and white grids on the chessboard. But for our study, thermal cameras are used for imaging, which sensitizes the infrared light emitted by objects for imaging and causes significant blur. To reduce the blur, remapping the color with steep gradients is performed. This helps the MATLAB single-camera calibrator tool, which is adopted for distortion compensation and the data sampling for the perspective transformation. The calibration process, including the metal chessboard and its thermal images, is shown in Figure 1. Comparing Figure 1(b), (c), and (d). It is apparent that the curved outlines are corrected with distortion compensation, and the tilt lines due to view angles are corrected with perspective transformation. The metal chessboard with 3 mm × 3 mm mesh is accurately captured in the final image shown in Figure 1(d). Each mesh is characterized by 30 pixels to link the pixel size with the physical size. The pixel size for the final calibrated thermal image is 100 μm. The characteristic length (i.e., printed filament width in straight-line) is 1 mm, which is 10 times of the pixel size in thermal images (0.1 mm). So it is believed the subtleness of extracted printed width under this pixel size chosen can be guaranteed. The overall mean projection error $R_e \leq 0.16$ pixel is estimated, indicating that the calibration is desirable.

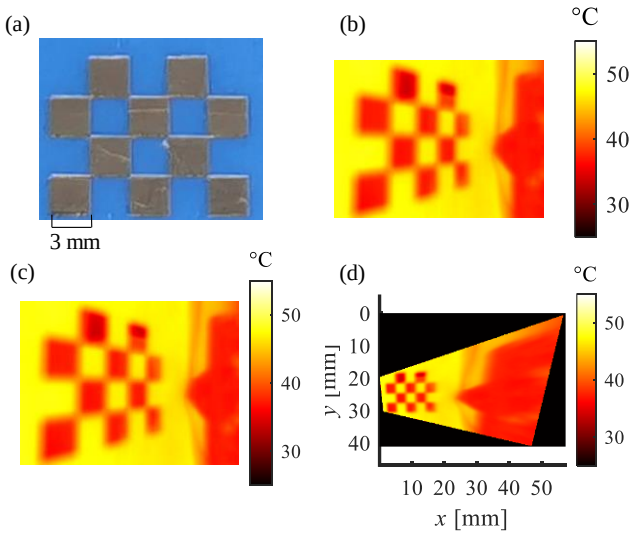

Figure 1: (a) Calibration Metal Mesh and Its Thermal Images: (b) Raw Image, (c) with Distortion Compensation, and (d) with Distortion and Perspective Transformation

3. IN-SITU MONITORING AND COMPENSATION OF MOTION AND EXTRUSION WITH THERMAL IMAGES

The in-situ thermal image of the AM process contains a lot of information, including the heat-affected region and the deposited path. Therefore, it has the potential to be extracted to evaluate the printing path deviation and extrusion inaccuracies. The estimated deviation and inaccuracy can be further exploited for motion and extrusion trajectory compensation.

3.1. Geometrical Printed Path Boundary Modeling and Critical Slender Deposition Condition

Assume the print head is moving along the trajectory $x(t), y(t)$ with flow rate $E(t)$, and the expected printing height is defined as h. The print head velocity $v(t)$ and the unit vector $e(t)$ representing the time-varying printing direction are defined as

$$v(t) = \{\dot{x}(t) \quad \dot{y}(t)\}^{\top}, \; e(t) = \frac{v(t)}{|v(t)|}. \tag{7}$$

It is desirable to know the exact boundary (including the left boundary $x_l(t), y_l(t)$ and right boundary $x_r(t), y_r(t)$) of the printed path for an arbitrary curve. The printing direction is constant when the trajectory is traveling straight. Assume the flow rate $E(t)$ is changing from t_0 to t_1 with steady-state initial and ending flow rate E_0 and E_1, the flow boundary condition should satisfy the following equation

$$Q = \int_{t_0}^{t} E(t)\,dt = 2h \int_{t_0}^{t} |v(t)|\,w(t)\,dt, \tag{8}$$

where Q is the total deposited filament volume and w is the half-width of the printed path. Since Eq. (8) needs to be satisfied for all t, the printing half-width can be derived as

$$w(t) = \frac{E(t)}{2h|v(t)|}. \tag{9}$$

Note that the printing half-width is constant when the flow rate and the printing velocity are constant.

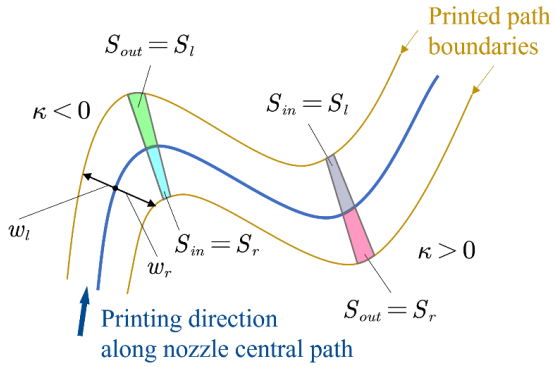

Figure 2: Width Calculation Illustration for Slender Deposition Path

Assume a time-varying trajectory with curvature $\kappa(t)$ calculated as

$$\kappa = \frac{x'y'' - x''y'}{(x'^2 + y'^2)^{\frac{3}{2}}}, \tag{10}$$

where x', x'', y' and y'' are the first- and second-order curve derivatives of the x and y axis, respectively. The curvature κ is positive for counterclockwise rotation in movement direction and is negative for clockwise movement. The radius of curvature is defined $\rho = 1/\kappa$. Along the printing direction $e(t)$, it is assumed that the material deposited on one side of the trajectory remains on one side. Consider the deposition process at a particular time instant as shown in Figure 2, S_l and S_r as the material deposition area on the left and right of the curve. Assuming the deposition process yields a slender curve (i.e., the major deposited material is perpendicular to the path center line), the deposited area on the left and the right of the curve center line along a small curve length ds is calculated as

$$S_l = w_l ds - \frac{1}{2} w_l^2 d\alpha = w_l \left(1 - \frac{w_l}{2}\kappa\right) ds, \tag{11}$$

$$S_r = w_r ds + \frac{1}{2} w_r^2 d\alpha = w_r \left(1 + \frac{w_r}{2}\kappa\right) ds, \tag{12}$$

where $d\alpha$ is the small change of the printing direction (positive value indicates counterclockwise rotation). Based on the assumption that the deposition on one side of the path centerline remains on this side, i.e.,

$$S_l = S_r = \frac{E}{2|v(t)|h} ds. \tag{13}$$

Combining Eqs. (11) to (13), the left and right printed half width satisfies the following equations

$$\frac{\kappa}{2} w_l^2 - w_l + \frac{E}{2|v(t)|h} = 0, \tag{14}$$

$$\frac{\kappa}{2} w_r^2 + w_r - \frac{E}{2|v(t)|h} = 0. \tag{15}$$

The solutions to these two equations are

$$w_l = \frac{1 - \sqrt{1 - \frac{\kappa E}{|v(t)|h}}}{\kappa}, \tag{16}$$

$$w_r = \frac{-1 + \sqrt{1 + \frac{\kappa E}{|v(t)|h}}}{\kappa}. \tag{17}$$

Note that Eqs. (14) and (15) only have real number solutions when a slender deposition condition is met, i.e.,

$$S_c \triangleq \left| \frac{\kappa E}{|v(t)|h} \right| \leq 1. \tag{18}$$

This is defined as the slender deposition condition. This indicates that the deposition process is mainly along the perpendicular direction of the center line, such that the deposited line is a slender curve. However, this slender deposition condition may not always hold, particularly for additive manufacturing cases where many linear segments are exploited. At the corners of the printed path, the curvature will be extremely large, and the slender deposition condition will be locally violated. This indicates that the printing deposition direction will no longer be perpendicular to the printing direction, and additional operations are needed to address this situation.

3.2. Curvature Smoothing and Deposition Direction Establishment

In order to address the large curvatures on the trajectory, additional rotational angles are introduced to ensure that the assumed deposition paths are not intersecting. At normal regions of the trajectory where the curvature is small (satisfying slender deposition condition in Eq. (18)), the deposition direction is perpendicular to the printing direction. However, when curvature is large, an additional rotation angle $\phi(t)$ is introduced. Its corresponding curvature is defined as

$$\kappa_\phi = \frac{d\phi}{ds} = \frac{d\phi}{dt}\frac{1}{v(t)}. \tag{19}$$

This rotation angle grants additional freedom to minimize the curvature for the slender deposition condition. Define the effective curvature as

$$\kappa_{eff} = \kappa + \kappa_\phi. \tag{20}$$

The slender deposition condition in Eq. (18) is modified to

$$S_c \triangleq \left| \frac{\kappa_{eff} E}{|v(t)|h} \right| \leq 1. \tag{21}$$

On the other hand, the design of κ_ϕ is not completely free. It needs to satisfy the rotation angle of the original trajectory, i.e., conditions

$$\begin{aligned} \int_0^{s_0} \kappa(s) ds &= \int_0^{s_0} (\kappa(s) + \kappa_\phi(s)) ds, \\ \int_0^{t_0} \kappa(t) v(t) dt &= \int_0^{t_0} (\kappa(t) + \kappa_\phi(t)) v(t) dt, \end{aligned} \tag{22}$$

are expected to hold for sufficient long s_0 and t_0. This can be achieved by redistribution of the high κ regions to its neighborhoods.

The detailed implementation first assumes $\kappa_\phi(t)=0$, and calculates the $S_c(t)$ value along the trajectory. The timespan where $S_c(t)$ continuously exhibiting larger than one absolute value is extracted. Define the first continuous timespan that violates Eq. (21) to be $\mathbf{t}_v$, corresponding $\kappa_\phi(t)$ values when $t\in\mathbf{t}_v$ are designed to enforce Eq. (21). To account for the rotation angle insufficiency, integration is defined as

$$\Delta\phi=\int_{t\in\mathbf{t}_v}\kappa_\phi(t)v(t)dt. \tag{23}$$

For the symmetry of the path, the value $\Delta\phi$ is cut in half and redistributed to its past and future of $\mathbf{t}_v$. This operation can be repeated until $\mathbf{t}_v=\emptyset$, indicating that the modified slender deposition condition Eq. (21) is satisfied for the entire trajectory. The results of the curve smoothing method and the generated principal deposition directions are illustrated in Figure 3. It can be seen that the estimated boundary expands at the cornering regions where κ is large, but the velocity is low. Also, the primary deposition directions (marked in red) are continuously distributed in the neighborhood of the cornering regions, thanks to the planning of $\kappa_\phi(t)$.

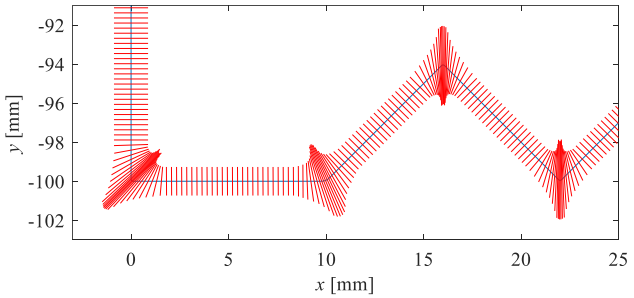

Figure 3: Curve Smoothing Method and the Generation of Principal Deposition Directions

3.3. Thermal Image Printing Information Extraction and extrusion compensation

An enhanced level of accuracy is needed to further extract the trajectory and extrusion information from the thermal image. For such purposes, the localization of the thermal image is needed. The localization and fine adjustment are achieved under an optimization framework. The optimization variable is defined as

$$z=\{x_n^{(im)},y_n^{(im)},t_i,M_{11},M_{12},M_{21},M_{22}\}^\top, \tag{24}$$

where $(x_n^{(im)},y_n^{(im)})$ is the location of the nozzle in the image coordinates, t_i is the accurate time instance that the thermal image is taken, and M is a secondary rotational matrix that serves the same purpose as the perspective transformation matrix M_t in Eq. (6). The optimization objective is to maximize the temperature within the heat affected region Ω_H and the effective image region Ω_I over a set of thermal images, i.e.,

$$J=\sum_i\int_{(x,y)\in\Omega_H\bigcap\Omega_I}|T_i(z)|dxdy, \tag{25}$$

where $T_i(z)$ is the i^{th} thermal image's temperature values. One exemplar localization example is shown in Figure 4. It can be seen that the heat-affected region Ω_H is assumed to be the neighborhood of the trajectory; the effective image region is assumed to be the left region in the original image, and is transformed into a polygon after the original perspective transformation M_t. The small tilting of the figure indicates that a small M is also introduced for the secondary transformation for the maximum alignment of the thermal image to the printing path. The resultant high-temperature regions align well with the printing path with the optimization.

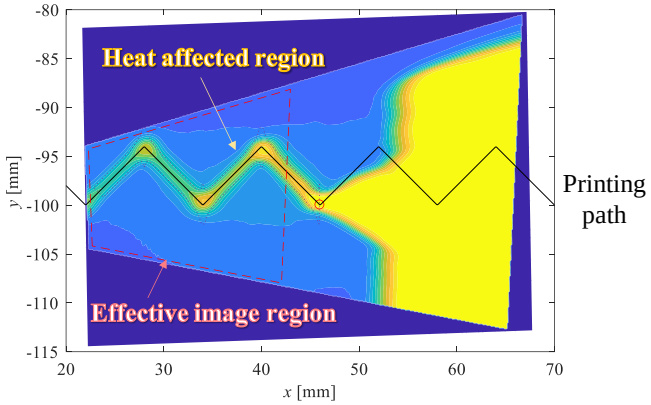

Figure 4: Localization of the Thermal Image

Note that the deposition direction calculated and plotted in Figure 3 formulates a set of boundary directions. Its intersection with the boundary of the thermal image yields an estimation of the actual printed trajectory. In other words, the terms $w_l(t)$ and $w_r(t)$ can be extracted.

To improve the accuracy of width extraction, cooling compensation which calculates the filament temperature $T(t_p,t_p)$ at printing time t_p from the temperature observed at the time t_o (i.e., $T(t_o,t_p)$) is applied. The relationship between $T(t_p,t_p)$ and $T(t_o,t_p)$ is assumed to satisfy the conventional exponential cooling law [27] as

$$T(t_o,t_p)-T_e=(T(t_p,t_p)-T_e)e^{-k_t(t_o-t_p)}, \tag{26}$$

where k_t is cooling constant and T_e is environmental temperature. Exploiting this relationship, the cooling compensation first converts the thermal image with printed

filament as shown in Figure 4 to a one-dimensional manifold that flows in time. The detailed procedure relies on the critical deposition direction defined in Figure 3. For an arbitrary point, the temperature when printing is derived from Eq. (26) as

$$T(t_p,t_p)=\frac{T(t_o,t_p)-T_e}{e^{-k_t(t_o-t_p)}}+T_e. \tag{27}$$

This procedure applies to the entire manifold and the temperature distribution with cooling compensation along the deposition direction crossing the corner region is shown in Figure 5. The over-extruded regions are conveniently extracted by temperature contour, correspondingly.

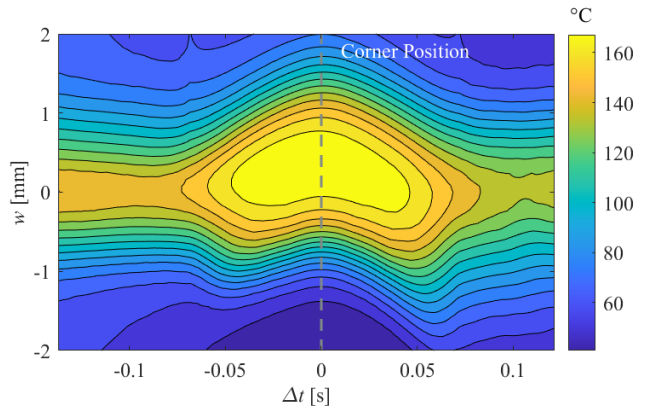

Figure 5: Temperature Distribution Converted to the Deposition Direction and Time

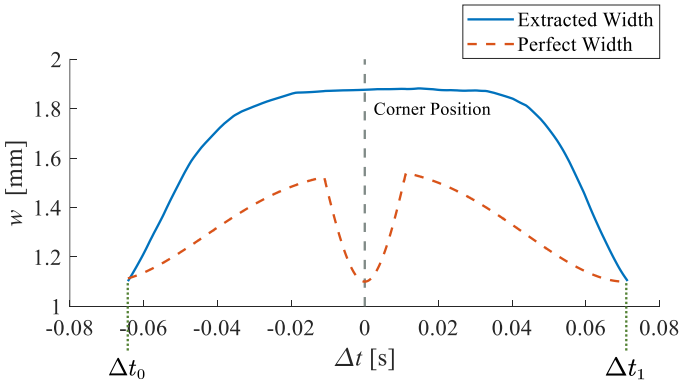

Figure 6: Extracted Printed Width and Desirable Printed Width in a Continuous Timespan

The contour threshold temperature T_t is critical to the final extracted region. This threshold is calibrated by the printing experiments in the straight line regions, where the left and right half width with different threshold temperatures T_t as $w_l(T_t,t)$ and $w_r(T_t,t)$ as a function of time. The T_t is thus selected by the minimization as

$$T_t=\operatorname{argmin}\{w_l(T_t,t)+w_r(T_t,t)-2w_a\}, \tag{28}$$

where w_a is the actual half-width of printed filament at a straight-line region. The contour with the specified threshold temperature T_t is used to obtain the extracted width $w_l(T_t,t)$ and $w_r(T_t,t)$ from Figure 5.

The printing timespan that needs extrusion compensation is located by comparing its left and right half width $w_l(T_t,t)$ and $w_r(T_t,t)$ with its desired width $w_d(t)$ defined in Eq. (30). Define the error of extrusion width Δw as

$$\Delta w(t)=w_l(T_t,t)+w_r(T_t,t)-2w_d(t). \tag{29}$$

Define ε as the maximum tolerable extrusion inaccuracy; $|\Delta w|\geqslant\varepsilon$ indicates an extrusion inaccuracy that needs to be compensated. Define Δt_0 and Δt_1 as starting and ending time of a continuous extrusion inaccuracy timespan, respectively. The extracted and perfect width in a continuous extrusion inaccuracy timespan collected from Figure 5 is shown in Figure 6. Contour is used to obtain the extracted width from Figure 5, helping to capture the over-extrusion in subpixel size.

The perfect half-width of a printed part along the deposition direction is given by

$$w_d(t)=\frac{w_0}{\cos(\phi(t))}, \tag{30}$$

where w_0 is the desirable printed path half-width for straight lines. From this information, the local over-extrusion rate is estimated to be

$$\Delta E(t)=K_e(w_l+w_r-2w_d), \tag{31}$$

where K_e is an extrusion correction gain acquired from experiments. This over-extrusion time-dependent trajectory can be used to estimate and compensate for the extrusion trajectory. The practical extrusion process involves a dynamic process. The reaction from the extrusion command $\Delta E(t)$ is the system output, while the reference command $\Delta E_r(t)$ is the system input. Following Bellini et al. [28], this extrusion reaction can be modeled with a first-order linear time-invariant (LTI) system, given by

$$\Delta E(s)=\underbrace{\frac{1}{\tau s+1}}_{G(s)}\Delta E_r(s), \tag{32}$$

where s is the Laplace variable, τ is the time constant. For such LTI system, the inverse relationship is acquired by

$$\Delta E_r(t)=\Delta E(t)+\tau\frac{d\Delta E}{dt}. \tag{33}$$

Since the image already contains the time sequence of $\Delta E(s)$, the derivative operation in Eq. (33) is typically performed with additional zero-phase low-pass filters. This extrusion trajectory can be used to compensate for the extrusion inaccuracy.

To account for the extrusion dynamics, the compensation velocity range is extended to from $\Delta\hat{t}_0$ to $\Delta\hat{t}_1$. The corresponding input extrusion compensation velocity trajectory $\Delta v_{er}(\Delta t)$ is smoothly parameterized with a non-uniform rational basis spline (NURBS) as

$$\Delta\hat{v}_{er}(\Delta t) = \sum_{i=0}^{n} N_{i,p}(\Delta t) P_i(\Delta t_i, \Delta v_{ei}), \tag{34}$$

where $N_{i,p}(\Delta t)$ is the basis function and P_i is the control point. To guarantee smooth transition with the uncompensated regions, the final input extrusion velocity $v_{ef}(\Delta t)$ satisfies $v_{ef}(\Delta t) = v_e(\Delta t) - \Delta v_{er}(\Delta t)$, where $v_e(\Delta t)$ is the origin input extrusion velocity.

Applying the transfer function $G(s)$ in Eq. (32) to $N_{i,p}(s)$, the filtered basis function $\widetilde{N}_{i,p}(s)$ is given by

$$\widetilde{N}_{i,p}(s) = G(s) N_{i,p}(s). \tag{35}$$

Accordingly, the desired output extrusion compensation velocity $\Delta\hat{v}_e(\Delta t)$ is calculated as in [29–31]

$$\Delta\hat{v}_e(\Delta t) = \sum_{i=0}^{n} \widetilde{N}_{i,p}(\Delta t) P_i(\Delta t_i, \Delta v_{ei}). \tag{36}$$

Define the perfect extrusion compensation velocity output as

$$\Delta v_e(t) = K_v \Delta w(\Delta t), \tag{37}$$

where K_v is an extrusion velocity correction gain identified from experiments. The control points $P_i(\Delta t_i, \Delta v_{ei})$ are calculated by

$$\begin{aligned} P_i(\Delta t_i, \Delta v_{ei}) &= \operatorname{argmin}\left\{ \| \Delta\hat{v}_e(\Delta t) - \Delta v_e(\Delta t) \|^2 \right\}, \\ \text{s.t. } & \Delta v_{\min} \le \Delta v_{ei} \le \Delta v_{\max}, \\ & P_0 = \left(\Delta\hat{t}_0, 0\right), \\ & P_n = \left(\Delta\hat{t}_1, 0\right). \end{aligned} \tag{38}$$

The range of Δv_{ei} is constrained considering origin extrusion velocity and extrusion dynamics with the minimum and maximum compensation velocity. Figure 7 shows the calculated result of desired input $\Delta\hat{v}_{er}(t)$ and perfect output $\Delta v_e(\Delta t)$ of extrusion compensation velocity.

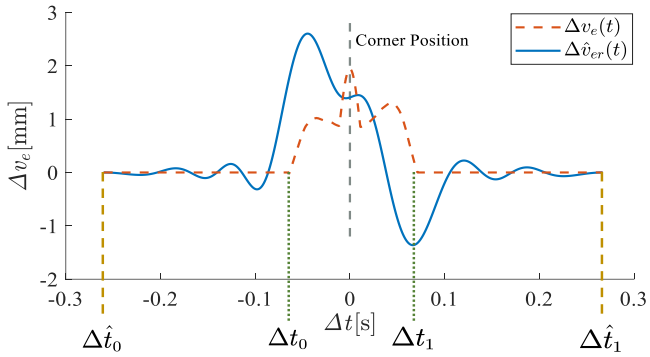

Figure 7: Extrusion Compensation Sequence

4. EXPERIMENTS

4.1. Experimental Setup

The Flashforge Creator 3 (whose printing size equals) is used for the experiments, as shown in Figure 8. Here a lightweight and firm fixture tightly fixes the thermal camera chip (FLIR 3.5) to the printing nozzle. The printing parameters and the camera specifications are specified in Table 1 and Table 2, respectively. Note that the thermal expansion of PLA in the targeted range is very small. A 200 °C drop in temperature only causes 0.0041% 1D shrinkage. Therefore, the thermal expansion in the thermal image is omitted in this case.

Table 1: Printing Parameters

Printer maximum size	300×250×200 mm^3
Printer name	Flashforge Creator 3
Nozzle diameter	0.4 mm
Layer height	0.2 mm
Printing speed	20 mm/s
Acceleration	500 mm/s^2
Corner tolerance	0.05mm
Printing material	PLA
Thermal expansion coefficient	41 μm/(m·K)
Nozzle temperature	230 °C
Print bed temperature	45 °C
Printing filament diameter	1.75 mm

Table 2: Thermal Camera Specifications

Type	FLIR 3.5
Frame rate	8 Hz
Minimum temperature	−10 °C
Maximum temperature	450 °C
Weight	0.9 gram
Resolution	160×120
Thermal sensitivity	<50 mK (0.050° C)
Tilt angle	45°
Distance to the printing plane	14.5 mm

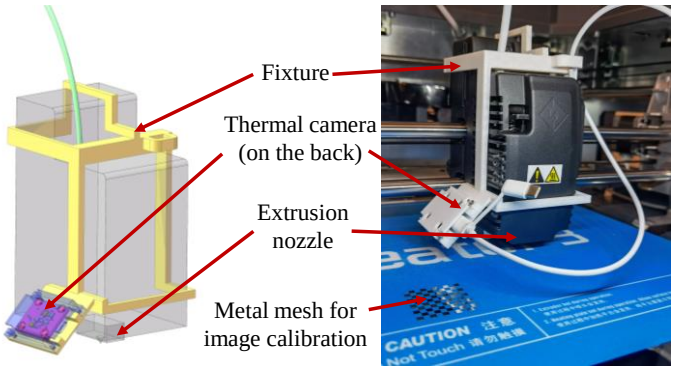

Figure 8: Experimental Setup with the Thermal Camera Chip Attached to the Extrusion Nozzle

4.2. Extrusion Dynamics Identification

The identification of the extrusion dynamics relies on the time-domain formulas of the LTI system defined in Eq. (32). The step response is written as

$$W(t) = W_2 + (W_1 - W_2)e^{\left(-\frac{t-t_0}{\tau}\right)}, \tag{39}$$

where $W(t)$ is the time-varying filament width, W_1 and W_2 are the initial width and final width under different extrusion speeds, respectively. To identify the extrusion dynamics during AM process, a 30 mm single track is deposited along the horizontal direction with a constant printing speed v of 10 mm/s. The feed deposit rate ratio α steps from 0.1 to 0.3 at the 10 mm position and decreases from 0.3 to 0.1 at the 20 mm position so that the extrusion rate changes from 3 mm/s to 9 mm/s and then to 3 mm/s accordingly. As shown in Figure 9(a), the testing part is printed in a white frame whose size is perfectly known. This helps with image calibration. A U-shape is adopted to guarantee sufficient extrusion at the initial position and help locate the starting time.

The deposited filament width information along the trajectory is captured by the camera and evaluated through image processing. For the setup in this experiment, the resolution of the measurements is 0.0632 mm/pixel. Then, the information-rich regions are extracted for edge detection with Canny filter. Edge points of the filament are extracted, and the parameters are calculated, as shown in Figure 9(b). The W_1, W_2, τ and t_0 are calculated by using constrained optimization in MATLAB according to the measured data and the fitted upper and lower extrusion boundaries. For this experiment, W_1 is 0.9357 mm, W_2 is 1.8019 mm, and τ is 0.0873 s. The W_1 and W_2 measured directly with a vernier caliper are 0.940 mm and 1.760 mm, respectively, which are consistent with the calculated value.

To further identify the influence of α on the filament width, filaments with different α are deposited. According to the same amount of the fed material and extruded material amount, the relationship between α and W can be written as

$$W = \pi R^2 \alpha / 2h = \beta\alpha, \tag{40}$$

where R is the radius of print material and β is a constant to describe the linear relationship between α and W. More values changing α from 0.1 to 0.35 are experimentally verified with their static values. The fitted data formulate a linear function, expressed as $W = p_1\alpha + p_2$. The results are shown in Figure 10. Variable p_1 equals 3.44 and p_2 equals 0.6693. The R^2 of this fit is more than 95%, indicating a desirable estimation. The extrusion velocity correction gain is experimentally determined to be $K_v = 2\ \mathrm{s}^{-1}$.

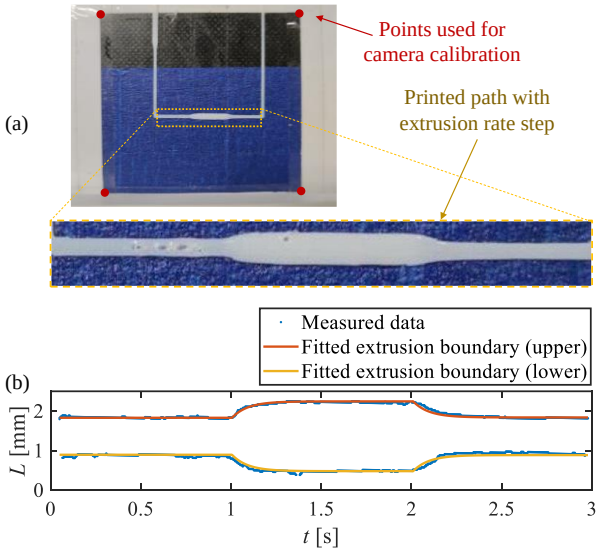

Figure 9: Identified Extrusion Dynamics: (a) Image of Printed part and (b) Extracted Boundary

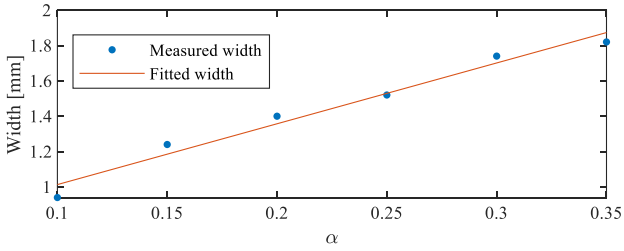

Figure 10: Relationship between α and Printed Width

4.3. In-situ Thermal Monitoring and Extrusion Trajectory Compensation

A 90-degree angle trajectory with repeated features was selected as a case study. The printing parameters are summarized in Table 1. The image, original, and calibrated thermal image is shown in Figure 11. It is clear that the corner region suffers from the over-extrusion issue. The reason for the over-extrusion arises from the fact that the lower speed and reduced areas to cover are not considered by the conventional trajectory planning software.

Therefore, slow movement and consistent extrusion contribute to more materials at the corner regions. Here we define an over-extrusion index O_E as

$$O_E = \frac{A_o}{A_c}, \tag{41}$$

where A_o is the over-extruded area, and A_c is the perfect corner polytope area in a corner. The minimum and maximum compensation velocities have been set to $\Delta v_{\min} = -2$ mm/s and $\Delta v_{\max} = 4$ mm/s, respectively. The actual contour extraction, over-extrusion area extraction, and compensation sequence generation have been shown in Figure 5, Figure 6, and Figure 7, respectively. The results before and after the compensation are shown in Figure 12. The over-extruded area A_o marked in red in Figure 12(c) is observed to be shrunk significantly. The corresponding over-extrusion index O_E for this print has dropped from 144.94% to 22.91%, indicating an enhancement in extrusion accuracy.

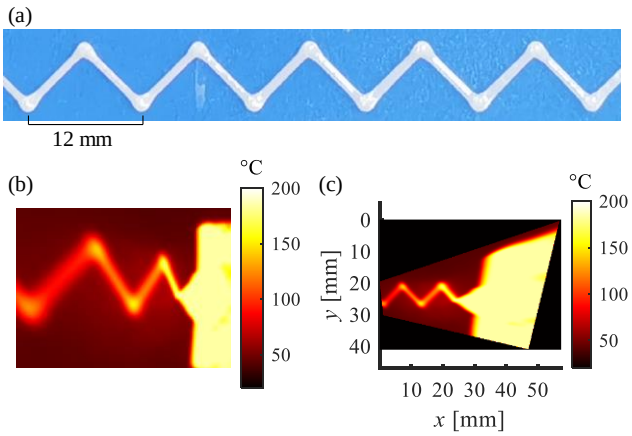

Figure 11: Representative In-situ Monitoring (a) its Thermal Images: (b) Raw Image, and (c) with Distortion and View Angle Compensation

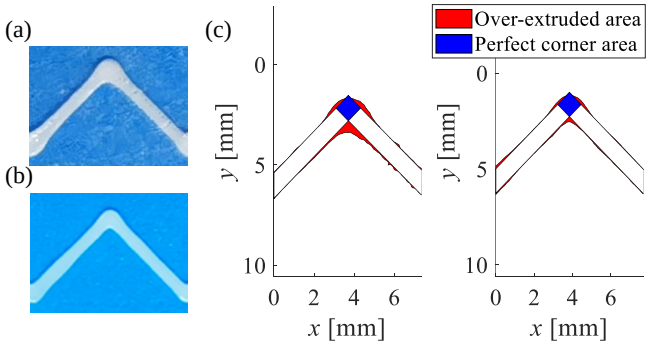

Figure 12: Printed Corners (a) before and (b) after the Compensation Methods, with Extracted Over-Extruded Area Highlighted in (c), Respectively

5. CONCLUSION

This paper proposed a set of thermal-image-enabled monitoring and trajectory extrusion control methods for the dynamic features of the additive manufacturing process.

- Thermal images are used to extract over-extrusion regions coupled with time-domain trajectory, which can be further converted to the command compensation signals to alleviate the over-extrusion issue.
- Experiments have been performed, showing that the over-extrusion index for the printed 90-degree corner decreased from 144.94% to 22.91%, demonstrating a significant improvement effect.
- Future work will focus on robustness and automation enhancements with more corning angles and speeds.

ACKNOWLEDGEMENTS

The authors acknowledge support from HKUST research equipment development fund and HKUST Bridge Gap Fund (BGF). This work was supported in part by the Project of Hetao Shenzhen-Hong Kong Science and Technology Innovation Cooperation Zone (HZQB-KCZYB-2020083). Profs. Baolin Huang, Kai Tang, and Xiaomeng Li provided valuable feedback to this work. The help from the funding agency and the other researchers is sincerely appreciated.

REFERENCES

[1] Gibson, I., Rosen, D., Stucker, B., and Khorasani, M., 2021, *Additive Manufacturing Technologies*, Springer International Publishing, Cham.

[2] Lhachemi, H., Malik, A., and Shorten, R., 2019, "Augmented Reality, Cyber-Physical Systems, and Feedback Control for Additive Manufacturing: A Review," IEEE Access, **7**, pp. 50119–50135.

[3] Everton, S. K., Hirsch, M., Stavroulakis, P. I., Leach, R. K., and Clare, A. T., 2016, "Review of In-Situ Process Monitoring and in-Situ Metrology for Metal Additive Manufacturing," Mater. Des., **95**, pp. 431–445.

[4] Patel, J., ed., 2019, *Data-Driven Modeling for Additive Manufacturing of Metals*, National Academies Press, Washington, D.C.

[5] Tapia, G., and Elwany, A., 2014, "A Review on Process Monitoring and Control in Metal-Based Additive Manufacturing," J. Manuf. Sci. Eng. Trans. ASME, **136**(6), pp. 1–10.

[6] Liu, S., Brice, C., and Zhang, X., 2021, "Comprehensive Quality Investigations of Wire-Feed Additive Manufacturing Based on Machine Learning of Experimental Data."

[7] Lee, J., and Prabhu, V., 2016, "Simulation Modeling for Optimal Control of Additive Manufacturing Processes," Addit. Manuf., **12**, pp. 197–203.

[8] Liu, Z., Zhang, H.-C., Peng, S., Kim, H., Du, D., and Cong, W., 2019, "Analytical Modeling and Experimental Validation of Powder Stream Distribution during Direct Energy Deposition," Addit. Manuf., **30**, p.

100848.
[9] Coogan, T. J., and Kazmer, D. O., 2017, "Bond and Part Strength in Fused Deposition Modeling," Rapid Prototyp. J., **23**(2), pp. 414–422.
[10] Prasad, A. K., Kapil, S., and Bag, S., 2022, "Critical Conditions for Melting of Metallic Wire in Induction Heating System through Numerical Simulation and Experiments," J. Manuf. Process., **77**, pp. 678–693.
[11] Razvi, S. S., Feng, S., Narayanan, A., Lee, Y. T. T., and Witherell, P., 2019, "A Review of Machine Learning Applications in Additive Manufacturing," Proc. ASME Des. Eng. Tech. Conf., **1**, pp. 1–10.
[12] Meng, L., McWilliams, B., Jarosinski, W., Park, H.-Y., Jung, Y.-G., Lee, J., and Zhang, J., 2020, "Machine Learning in Additive Manufacturing: A Review," JOM, **72**(6), pp. 2363–2377.
[13] Gardner, J. M., Hunt, K. A., Ebel, A. B., Rose, E. S., Zylich, S. C., Jensen, B. D., Wise, K. E., Siochi, E. J., and Sauti, G., 2019, "Machines as Craftsmen: Localized Parameter Setting Optimization for Fused Filament Fabrication 3D Printing," Adv. Mater. Technol., **4**(3), pp. 1–10.
[14] Jiang, J., Yu, C., Xu, X., Ma, Y., and Liu, J., 2020, "Achieving Better Connections between Deposited Lines in Additive Manufacturing via Machine Learning," Math. Biosci. Eng., **17**(4), pp. 3382–3394.
[15] Wang, C., Tan, X. P., Tor, S. B., and Lim, C. S., 2020, "Machine Learning in Additive Manufacturing: State-of-the-Art and Perspectives," Addit. Manuf., **36**(August), p. 101538.
[16] Qi, X., Chen, G., Li, Y., Cheng, X., and Li, C., 2019, "Applying Neural-Network-Based Machine Learning to Additive Manufacturing: Current Applications, Challenges, and Future Perspectives," Engineering, **5**(4), pp. 721–729.
[17] Baturynska, I., Semeniuta, O., and Martinsen, K., 2018, "Optimization of Process Parameters for Powder Bed Fusion Additive Manufacturing by Combination of Machine Learning and Finite Element Method: A Conceptual Framework," Procedia CIRP, **67**, pp. 227–232.
[18] Zhao, X., Landers, R. G., and Leu, M. C., 2010, "Adaptive Extrusion Force Control of Freeze-Form Extrusion Fabrication Processes," J. Manuf. Sci. Eng., **132**(6).
[19] Zomorodi, H., and Landers, R. G., 2016, "Extrusion Based Additive Manufacturing Using Explicit Model Predictive Control," *American Control Conference*, American Automatic Control Council (AACC), pp. 1747–1752.
[20] Deuser, B. K., Tang, L., Landers, R. G., Leu, M. C., and Hilmas, G. E., 2013, "Hybrid Extrusion Force-Velocity Control Using Freeze-Form Extrusion Fabrication for Functionally Graded Material Parts," J. Manuf. Sci. Eng., **135**(4), pp. 1–11.
[21] Purtonen, T., Kalliosaari, A., and Salminen, A., 2014, "Monitoring and Adaptive Control of Laser Processes," Phys. Procedia, **56**, pp. 1218–1231.
[22] Thirumarimurugan, M., Subramanian, S. S., and Ramasubramanian, M., 2016, "Performance Process Evaluation of Extrusion," J. Appl. Sci. Res., **12**(3), pp. 65–70.
[23] Abeykoon, C., Li, K., Mcafee, M., Martin, P. J., and Irwin, G. W., 2011, "Extruder Melt Temperature Control with Fuzzy Logic," *18th World Congress The International Federation of Automatic Control*, IFAC, Milano, Italy, pp. 8577–8582.
[24] Abeykoon, C., 2014, "A Novel Model-Based Controller for Polymer Extrusion," IEEE Trans. Fuzzy Syst., **22**(6), pp. 1413–1430.
[25] Grimard, J., Dewasme, L., and Wouwer, A. Vande, 2017, "Dynamic Modeling and Model-Based Control of a Twin Screw Extruder," *25th Mediterranean Conference on Control and Automation*, IEEE, pp. 316–321.
[26] Zhang, Z., 2000, "A Flexible New Technique for Camera Calibration," IEEE Trans. Pattern Anal. Mach. Intell., **22**(11), pp. 1330–1334.
[27] Mills, A. F., 1992, *Heat Transfer*, CRC Press.
[28] Bellini, A., Güçeri, S., and Bertoldi, M., 2004, "Liquefier Dynamics in Fused Deposition," J. Manuf. Sci. Eng. Trans. ASME, **126**(2), pp. 237–246.
[29] Chou, C.-H., Duan, M., and Okwudire, C. E., 2023, "A Physics-Guided Data-Driven Feedforward Tracking Controller for Systems with Unmodeled Dynamics – Applied to 3D Printing," IEEE Access.
[30] Duan, M., Yoon, D., and Okwudire, C. E., 2018, "A Limited-Preview Filtered B-Spline Approach to Tracking Control – with Application to Vibration-Induced Error Compensation of a 3D Printer," Mechatronics, **56**, pp. 287–296.
[31] Ramani, K. S., Duan, M., Okwudire, C. E., and Ulsoy, A. G., 2019, "Optimal Selection of Basis Functions for Minimum-Effort Tracking Control of Nonminimum Phase Systems Using Filtered Basis Functions," J. Dyn. Syst. Meas. Control, **141**(11).

